

A new method for simulating rigid body motion in incompressible two-phase flow

Jessica Sanders¹, John E. Dolbow¹, Peter J. Mucha² and Tod A. Laursen^{1,*},[†]

¹*Duke Computational Mechanics Laboratory, Pratt School of Engineering,
Duke University, Durham, NC 27707, U.S.A.*

²*Department of Mathematics, University of North Carolina, Chapel Hill, NC 27599, U.S.A.*

SUMMARY

Computational treatment of immersed rigid bodies, especially in the presence of free surfaces and/or breaking waves, poses several modeling challenges. A motivating example where these systems are of interest is found in offshore wave energy harvesting systems, where a floating structure converts mechanical oscillations to electrical energy. In this study, we take the first step in developing a robust computational strategy for treating rigid bodies with possible internal dynamics, such that they may be fully coupled to a fluid environment with free surfaces and arbitrarily large fluid motion.

Many schemes for fluid–solid interaction involve formulating and solving all of the equations of motion on a structured cartesian finite difference grid, but with overlaying Lagrangian representation of the solid that is used to track its position. Ultimately, most of these techniques, which include methods for deformable solids as well, solve the equations of motion completely on the Eulerian grid (see, for example, (*J. Comput. Phys.* 2005; **205**:439–457) and (*J. Comput. Phys.* 2008; **227**:3114–3140)). By contrast, we solve Lagrangian-type rigid body equations coupled with the Eulerian formulation of the Navier Stokes equations for an immersed solid. This departure from the standard method facilitates the addition of the internal dynamics characteristic of power conversion systems. The study is based on a finite difference and level set description of a free surface between two immiscible fluids (for example water and air) for incompressible flow by Summan (*J. Comput. Phys.* 1994; **114**:146–159). Copyright © 2010 John Wiley & Sons, Ltd.

Received 21 December 2009; Revised 2 June 2010; Accepted 5 June 2010

KEY WORDS: fluid–structure interaction; rigid bodies; two-phase flow; wave energy

1. INTRODUCTION

The objective of this study is to present a robust numerical algorithm for the simulation of rigid structures interacting with incompressible two-phase viscous fluid flow in the presence of free surfaces. The numerical method is formulated in such a way that extra attenuating forces and internal dynamics can be easily introduced into the rigid body equations of motion. A motivating example where these systems might be of interest is offshore wave energy harvesting systems in which a floating structure converts mechanical oscillations to electrical energy. Several sophisticated approaches exist for rigid body interaction with flow described by the full Navier Stokes equations, but until now few or none of these approaches solve the rigid body equations of motion in a fully Lagrangian sense.

*Correspondence to: Tod A. Laursen, Department of Mechanical Engineering and Materials Science, Duke University, Durham, NC 27708-0300, U.S.A.

[†]E-mail: laursen@duke.edu

Many of the challenges of fluid/structure interaction have been addressed in the numerical methods community (see for example [1–4]). In general terms, it is more common for the computational fluid dynamics (CFD) community to apply finite difference techniques in an Eulerian framework to the spatial discretization of the Navier Stokes equations. There has also been a recent effort within the finite difference community to accurately resolve free surfaces and two-phase flows [5]. For solid mechanics, on the other hand, the numerical community usually employs Finite Element Analysis with Lagrangian coordinate systems.

This study has been developed with an eye towards employing the full benefits of both the Eulerian and Lagrangian coordinate systems for the analysis of fluids and solids, respectively. It is built upon existing techniques for the robust representation of free surfaces in two-phase flow with finite differences (see, for example, [5]), and introduces the idea that both Eulerian and Lagrangian frameworks may be used to formulate and solve equations of motion, thus inheriting the advantages of both schemes. It is our intent that the computation strategy presented herein be extendable in a robust manner to the analysis of deformable bodies under Lagrangian coordinates, embedded in an Eulerian fluid framework.

Many schemes for fluid–structure interaction involve formulating and solving all of the equations of motion on a structured cartesian finite difference grid. In these methods, overlaying Lagrangian representations of the solid track its location, but are not used explicitly to update its position. Techniques have been developed for transferring forces or representing constraints from an overlapping solid reference frame to the fluid reference frame. Immersed boundary methods, pioneered in the 1970s by Charles Peskin to model blood flow in the heart (see [1]), represent the action of the solid on the fluid as singular forces applied at fluid nodes in the region of an interface. In Peskin's methods and extensions such as the Immersed Finite Element Method [6], an immersed solid is advected with a background fluid velocity. A stress is thus generated in the solid and calculated with some constitutive relationship, after which the forces are appropriately transferred back to the fluid grid for subsequent time steps. Though the methods were developed for generally deformable bodies, very stiff constitutive relationships, or other modifications, are used to approximate rigid body motion [6, 7].

In a different approach, fictitious domain methods, or domain-embedding methods, have been applied to fluid–structure interaction in various ways starting with the study by Glowinski in the early 1990s [8–10]. Also referred to as Distributed Lagrange Multiplier approaches, fictitious domain methods simplify a geometrically irregular domain for a partial differential equation by extending the computational domain to a larger, more geometrically regular, region and applying boundary conditions on the original boundary. Glowinski applied the method to rigid particles in a fluid flow by ‘filling’ the rigid particle domains with fluid, solving the equations of motion on the entire domain and enforcing rigidity of the fluid in the particle domain through a Lagrange multiplier field. The multiplier can be seen as a body force required to enforce the rigidity constraint on the particles. By formulating the equations of motions of the fluid simultaneously with the equations of the particles and solving them together, boundary conditions between the two cancel out and are never explicitly calculated. Glowinski's methods are based on finite elements. The Rigid Fluid Method [11] is a finite difference approach based on the same principles implemented in the presence of a model-free surface (simulating single-phase fluid motion). In all of the preceding methods the equations of motion for both the solid and fluid are calculated on an Eulerian grid. Though Lagrangian coordinates may be employed to track the motion of a solid, and postcalculate stresses, they are not used to calculate the motion or deformation itself, as would normally be done for rigid body or solid mechanics problems. The paradigm of these methods is that the solid is advected with the fluid motion.

A more recent body of work has begun by studying rigid body/fluid interaction using Lagrangian equations of motion for the rigid body. Some aspects of two-way fluid/structure interaction with Lagrangian bodies have been recently introduced in the graphics community, with emphasis on speed and without quantitative evaluation [12–14]. Additionally, an immersed boundary method is proposed in [15], in which the equations of motion for the body are formulated in a non-inertial frame of reference. The method would be difficult to extend to multiple moving bodies in a given

flow. The authors of [16] have also proposed a method with Lagrangian equations of motion for rigid bodies in a fully three-dimensional flow, and have included a study of the effects of strong versus loose coupling of the fluid and rigid body equations. In this study we propose a fundamentally different method of formulating the forcing terms of the rigid body equations.

The following method will use the fully Lagrangian equations of motion to solve for the position and velocity of the rigid body, and in a reversal of the usual approach, the local fluid will be constrained to move with the calculated solid motion. Our approach has several advantages:

- For rigid particles, it is trivial to include the effects of the dynamics of mechanisms, including (for example) attached springs, dampers, and masses.
- In addition to fully coupled fluid/solid motion, the method can be easily applied to the one-way coupled problem in which the prescribed motion of a body forces the motion of the surrounding fluid. An example of this type will be presented in this paper, where the wave train in a wave tank is driven by an oscillating wedge.
- In the case of deformable solids, for which the method is intended to be extensible, a Lagrangian equation of motion would facilitate the full use of finite elements with all of the advantages therein, especially in cases where the strength of the material is of primary importance.
- Fully Eulerian schemes must interpolate values of a fluid velocity onto a solid domain. In the case of finite differences, it is not necessarily clear what a proper interpolation scheme would be, whereas the interpolation from a Lagrangian rigid body or a deformable finite element mesh onto fluid nodes is trivial, as in those cases the value of the velocity field is known *a priori*.

For the scope of this study, with wave energy harvesters as the motivating application, the most important advantage may be the lack of need to interpolate any fluid values onto the solid domain in order to advect it. For continued study, the ease of representation of complicated internal dynamics, including multiple interconnected spring mass systems, as well as power conversion systems that act to damp the mechanical motion, will also be of primary importance. The current scheme is benchmarked in two dimensions, but presented in a general way such that the algorithm is extendable to three-dimensional flows. The solid/fluid interaction method has been built upon stable and spatially second-order techniques for incompressible two-phase flow [17, 18].

2. GOVERNING EQUATIONS

2.1. Two-phase incompressible flow in an Eulerian framework

We consider a 2D fluid domain, Ω , with boundary $\partial\Omega$ as depicted in Figure 1. The differential equations of conservation of momentum in a continuum for a fluid are

$$\rho_f \left(\frac{D\mathbf{u}}{Dt} \right) = \nabla \cdot \boldsymbol{\sigma}_F + \rho_f \mathbf{g} \quad (1)$$

where ρ_f is the density of the fluid, \mathbf{u} is the velocity of the fluid, and $\boldsymbol{\sigma}_F$ is the fluid stress. For an incompressible Newtonian viscous fluid, the stress is taken to be a combination of hydrostatic and shear components,

$$\boldsymbol{\sigma}_F = -p\mathbf{I} + \mu_f(\nabla\mathbf{u} + \nabla^T\mathbf{u}) \quad (2)$$

where p is the hydrostatic pressure in the fluid and μ_f is the viscosity. Substitution of the fluid stress into the momentum equation for an Eulerian framework, and including a condition on conservation of mass, gives the familiar Navier Stokes equations for fluid velocity and pressure, which are

$$\rho_f \left(\frac{\partial\mathbf{u}}{\partial t} + \mathbf{u} \cdot \nabla\mathbf{u} \right) = -\nabla p + \mu_f(\Delta\mathbf{u}) + \rho_f \mathbf{g} \quad (3)$$

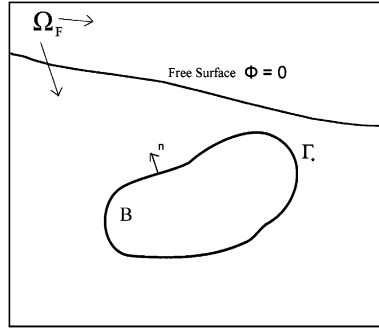


Figure 1. Two-dimensional domain including two-phase boundary ($\phi=0$) and rigid body, B .

and

$$\nabla \cdot \mathbf{u} = 0. \quad (4)$$

In the Level Set Method [5] for tracking two-phase flow, the conservation of momentum for the fluid is given as

$$\rho_f \left(\frac{\partial \mathbf{u}}{\partial t} + \mathbf{u} \cdot \nabla \mathbf{u} \right) = -\nabla p + \mu_f (\Delta \mathbf{u}) + \rho_f \mathbf{g} + \tau \kappa \delta(d) \mathbf{n} \quad (5)$$

where the last term represents a local surface tension force concentrated at the location of the phase interface. In this notation τ is the surface tension, κ is the curvature of the interface, \mathbf{n} is the surface normal at the interface, and $\delta(d)$ is the Dirac delta function at the location of the interface. The location between the phases is tracked as the zero contour of a scalar-valued function $\phi(\mathbf{x})$ which is advected with the fluid flow:

$$\frac{\partial \phi}{\partial t} + \mathbf{u} \cdot \nabla \phi = 0 \quad (6)$$

At any position, \mathbf{x} , where $\phi(\mathbf{x}) > 0$ the fluid is considered to be in a liquid phase, and the gas phase exists where $\phi(\mathbf{x}) < 0$. Fluid properties such as density or viscosity in either phase can then be expressed as a function of location in the domain. For example, in the case of density,

$$\rho_f = \rho_l H(\phi) + \rho_g (1 - H(\phi)) \quad (7)$$

where the function $H(\phi(\mathbf{x}))$ is

$$H(\phi(\mathbf{x})) = \begin{cases} 0 & \phi < 0 \\ 1 & \phi > 0 \end{cases}.$$

A similar expression holds for viscosity. Finally, the system of PDE's is completed through appropriate boundary and initial conditions on velocity and pressure.

2.2. Rigid body equations of motion

The Lagrangian equations of motion for an immersed rigid body, B , with boundary Γ^* completely immersed in Ω , are given by

$$m \frac{d\mathbf{v}}{dt} = \int_{\Gamma^*} \mathbf{t} d\Gamma^* + m\mathbf{g}, \quad (8)$$

and

$$I \frac{d\boldsymbol{\omega}}{dt} = \int_{\Gamma^*} (\mathbf{r} \times \mathbf{t}) d\Gamma^*, \quad (9)$$

where m is the solid mass, I is the rigid body rotational inertia, \mathbf{v} is the body's translational velocity, $\boldsymbol{\omega}$ is the rigid body angular velocity around the center of mass, and \mathbf{r} is the position vector from the center of mass to a point on the solid boundary Γ^* . The forcing terms on the particle are given as a combination of surface forces, \mathbf{t} , and body forces, in this case assumed to be gravity. Our challenge, which is avoided in existing methods where these equations are folded completely into an Eulerian framework, is to determine the functional form of the forcing, \mathbf{t} , on the particles from the physical coupling with the surrounding fluid.

2.3. No-slip boundary between solid and fluid

The fluid and solid equations are coupled through a no-slip condition

$$\mathbf{u} = \mathbf{v} + (\mathbf{r} \times \boldsymbol{\omega}) \quad \text{on } \Gamma^*. \quad (10)$$

In addition there is a balance of stresses

$$\boldsymbol{\sigma}_f \mathbf{n} = \mathbf{t} \quad \text{on } \Gamma^* \quad (11)$$

which states that the traction on the solid surface is equal to the fluid stress acting in the direction of the surface normal at any point on the particle boundary. Initial conditions on the particle position, \mathbf{d}_0 , and velocity, \mathbf{v}_0 , complete the physical system.

3. FLUID/SOLID INTERACTION MODEL

As with many numerical schemes (see, for example, [6, 8–11]) we approach the problem by first filling the solid domain with artificial fluid, which will be used to facilitate the interaction between the two. The kinematic boundary condition on the interface between the solid and fluid is extended to the entire domain of the artificial fluid:

$$\mathbf{u} = \mathbf{v} + (\mathbf{r} \times \boldsymbol{\omega}) \quad \text{on } B \quad (12)$$

Additionally, the dynamic boundary condition is expanded to indicate that the values of fluid stress both interior and exterior to the particle domain must be equal to the surface traction and each other at the particle interface:

$$\boldsymbol{\sigma}_F^i \mathbf{n} = \boldsymbol{\sigma}_F^o \mathbf{n} = \mathbf{t} \quad \text{on } \Gamma^* \quad (13)$$

The superscript i indicates a value that is supported only interior to the particle domain B , in the artificial fluid. Similarly, a superscript o will indicate a fluid property in the domain exterior to the particle (i.e. $\Omega \setminus B$). The balance of stresses (13) allows us to determine the forcing terms for the rigid body equations of motion. We substitute the fluid stress for the solid traction over the interface Γ^* in (8) and (9) to yield

$$m \frac{d\mathbf{v}}{dt} = \int_{\Gamma^*} (\boldsymbol{\sigma}_F \mathbf{n}) d\Gamma^* + m \mathbf{g} \quad (14)$$

and

$$I \frac{d\boldsymbol{\omega}}{dt} = \int_{\Gamma^*} \mathbf{r} \times (\boldsymbol{\sigma}_F \mathbf{n}) d\Gamma^*. \quad (15)$$

Here we have the choice of either $\boldsymbol{\sigma}_F^i$ or $\boldsymbol{\sigma}_F^o$; they are equivalent on the boundary via (13). Equation (14) is converted to a volume integral through simple application of the divergence theorem:

$$m \frac{d\mathbf{v}}{dt} = \int_B (\nabla \cdot \boldsymbol{\sigma}_F) dB + m \mathbf{g} \quad (16)$$

which is equivalent, through (1), to

$$m \frac{d\mathbf{v}}{dt} = \int_B \left\{ \rho_f \left(\frac{D\mathbf{u}}{Dt} \right) - \rho_f \mathbf{g} \right\} dB + m \mathbf{g}. \quad (17)$$

Additionally, it can be shown, given the symmetry of σ_F , that (15) is equivalent to

$$I \frac{d\boldsymbol{\omega}}{dt} = \int_B \mathbf{r} \times \left\{ \rho_f \left(\frac{D\mathbf{u}}{Dt} \right) - \rho_f \mathbf{g} \right\} dB. \quad (18)$$

The complete equations of motion for the coupled system are then given by (5) for the fluid in the domain $\Omega \setminus B$, (12) for the fluid in the domain B , and (17) and (18) for the motion of the rigid bodies.

4. NUMERICAL METHOD

4.1. Time integration scheme

Given a set of initial conditions for the fluid domain, \mathbf{u}_n , and p_n , and the rigid body, \mathbf{d}_n , \mathbf{v}_n , we wish to advance the solution of all the variables from $t = n$ to $t = n + 1$. Time integration is based on a classic Chorin pressure projection scheme [19]. First, an intermediate velocity is calculated over the entire domain Ω .

$$\mathbf{u}^* = \mathbf{u}^n + \Delta t \left[-\frac{\mathbf{u}^n \cdot \nabla \mathbf{u}^n}{\rho_f} + \frac{\mu_f (\Delta \mathbf{u}^n)}{\rho_f} + \frac{\tau \kappa \delta(d) \mathbf{n}}{\rho_f} + \mathbf{g} \right] \quad (19)$$

followed by a pressure projection step for p^{n+1} , again, in the entire domain,

$$\frac{\nabla^2 p^{n+1}}{\rho} = \frac{\nabla \cdot \mathbf{u}^*}{\Delta t} \quad (20)$$

and finally a correction to the velocity field,

$$\hat{\mathbf{u}} = \mathbf{u}^* + \frac{\Delta t \nabla p^{n+1}}{\rho_f}. \quad (21)$$

The solution is now divergence free, but does not represent a rigid velocity field in the domain, B . Everywhere else in the domain $\mathbf{u}^{n+1} = \hat{\mathbf{u}}$. The last step would be to advance the solution in that domain from $\hat{\mathbf{u}}$ to \mathbf{u}^{n+1} . In fact, this is a trivial step, because we know that the velocity field in B will be given by the particle velocity \mathbf{v}^{n+1} . This is a point of fundamental departure from the previous rigid body/fluid techniques, which advect the rigid body with the fluid, and compute forces on the background fluid mesh. In our case, we are advecting the fluid with the solid motion, and calculating forces which are applied to the solid equations of motion. To compute that particle velocity, however, we do need to be able to calculate the quantity

$$\int_B \left[\rho_f \frac{D\mathbf{u}^{n+1}}{Dt} - \rho_f \mathbf{g} \right] dB$$

It will be demonstrated that this can be computed with knowledge of the solution in the rest of the fluid field. As a point of notation, $\hat{\boldsymbol{\sigma}}$ should be understood to be the fluid stress (2) at the intermediate time step \hat{t} .

If the fluid stress for the artificial and real fluid is balanced on the boundary between them:

$$\boldsymbol{\sigma}_F^i \mathbf{n} = \boldsymbol{\sigma}_F^o \mathbf{n} = \mathbf{t} \quad \text{on } \Gamma^* \quad (22)$$

it follows that the integrals are also equal over the interface.

$$\int_{\Gamma} \boldsymbol{\sigma}_F^i \mathbf{n} d\Gamma = \int_{\Gamma} \boldsymbol{\sigma}_F^o \mathbf{n} d\Gamma \quad \text{on } \Gamma^* \quad (23)$$

The last step of the fluid solve, going from $\hat{\mathbf{u}}$ to \mathbf{u}^{n+1} , will only affect the velocity field in the artificial fluid, meaning $\hat{\mathbf{u}} = \mathbf{u}^{n+1}$ outside the particle domain, thus,

$$\int_B \left[\rho_f \frac{D\mathbf{u}^{n+1}}{Dt} - \rho_f \mathbf{g} \right] dB = \int_{\Gamma^*} \boldsymbol{\sigma}_F^{i,n+1} \mathbf{n} d\Gamma^* \quad (24)$$

$$= \int_{\Gamma^*} \boldsymbol{\sigma}_F^{o,n+1} \mathbf{n} d\Gamma^* \quad (25)$$

$$= \int_{\Gamma^*} \hat{\boldsymbol{\sigma}}_F \mathbf{n} d\Gamma^* \quad (26)$$

$$= \int_B \left[\rho \frac{D\hat{\mathbf{u}}}{Dt} - \rho \mathbf{g} \right] dB \quad (27)$$

In other words, the results of the integral on the left side of Equation (24), which is needed to complete the rigid body equations of motion, can be known from an evaluation of the equivalent integral at the intermediate time \hat{t} . The term $D\hat{\mathbf{u}}/Dt = \partial\hat{\mathbf{u}}/\partial t + \hat{\mathbf{u}} \cdot \nabla \hat{\mathbf{u}}$ is divided into inertial and convective components. The inertial term is discretized with a forward Euler strategy consistent with the rest of the method, $\partial\hat{\mathbf{u}}/\partial t = (\hat{\mathbf{u}} - \mathbf{u}^n)/\Delta t$. Similar expressions to (27) may be used, as desired, to couple fluid forces to solids which are deformable or have internal dynamics.

The time advancement algorithm, including a central difference approach to the rigid body equations, can now be described. For simplicity, only the translational rigid body equations will be presented, but the details of the exponential map used to update the rotational motions can be found in [20]. In brief, an exponential map of large rigid body rotations is employed to solve for the rotational velocity $\boldsymbol{\omega}$ and acceleration $\boldsymbol{\alpha}$, providing an algorithmic approach directly analogous to the central difference technique described below for rigid body translational degrees of freedom. The scheme is staggered, with the fluid velocity solved at time steps $n - 1/2$ and $n + 1/2$ and the particle variables solved at steps $n - 1/2, n, n + 1/2$, and $n + 1$. Additionally, the level set equation is advanced with a fourth-order Runge Kutta scheme.

Given initial conditions $\mathbf{u}_{n-1/2}, \mathbf{d}_n, \mathbf{v}_{n-1/2}$ in a typical time step, the algorithm may be summarized as follows:

1. Calculate the initial acceleration of the rigid body,

$$\mathbf{a}^n = \frac{\mathbf{f}^n(\mathbf{d}^n, \mathbf{u}^{n-1/2})}{m}, \quad (28)$$

where for the first time step only, $\mathbf{u}^{n-1/2} = \mathbf{u}^0$, and the right side forcing \mathbf{f}^n is given by the right side of Equation (17).

2. Update the particle velocity, \mathbf{v} and $\boldsymbol{\omega}$,

$$\mathbf{v}^{n+1/2} = \mathbf{v}^{n-1/2} + \Delta t \mathbf{a}^n. \quad (29)$$

3. Update the particle position,

$$\mathbf{d}^{n+1} = \mathbf{d}^n + \Delta t \mathbf{v}^{n+1/2}. \quad (30)$$

4. Set intermediate velocities equal in B ,

$$\mathbf{u}^{n+1/2} = \mathbf{v}^{n+1/2} + (\mathbf{r} \times \boldsymbol{\omega}^{n+1/2}) \quad \text{in } B. \quad (31)$$

The value of $\mathbf{u}^{n+1/2}$ in the domain B is imposed as a boundary condition for the fluid velocity within the domain overlapped by the solid.

5. Solve for an intermediate fluid velocity ,

$$\mathbf{u}^* = \mathbf{u}^{n-1/2} + \Delta t \left[-\frac{\mathbf{u}^{n-1/2} \cdot \nabla \mathbf{u}^{n-1/2}}{\rho_f} + \frac{\mu_f(\Delta \mathbf{u}^{n-1/2})}{\rho_f} + \mathbf{g} \right]. \quad (32)$$

6. Complete a pressure projection step,

$$\frac{\nabla^2 p}{\rho_f} = \frac{\nabla \cdot \mathbf{u}^*}{\Delta t}. \quad (33)$$

7. Correct the final fluid velocity,

$$\mathbf{u}^{n+1/2} = \mathbf{u}^* + \frac{\Delta t \nabla p}{\rho_f}. \quad (34)$$

8. Solve the level set equation and update the free surface position.

9. Next time step: increment $n+1 \Rightarrow n$, and $n+1/2 \Rightarrow n-1/2$ and return to Step 1.

For any explicit scheme there is a time step restriction to maintain stability. In this case, the time step is taken to be the lesser of the convective (Δt^{conv}) and viscous (Δt^{visc}) stable time steps, where

$$\Delta t^{\text{conv}} = \frac{C}{\left(\frac{u_{\max}}{\Delta x} + \frac{v_{\max}}{\Delta y} \right)} \quad (35)$$

and

$$\Delta t^{\text{visc}} = \frac{1}{2 * \left[\left(\frac{\mu_f}{\rho_f} \right)_{\max} \left(\frac{1}{\Delta x^2} + \frac{1}{\Delta y^2} \right) \right]}. \quad (36)$$

For all of the numerical examples, the stable time step is recalculated at every step.

The preceding time integration scheme represents a loose coupling between the equations of motion for the rigid bodies and fluid. That is to say, the forcing terms for the rigid body equations are dependent only on the location of the body at the preceding time step. A loose coupling strategy is computationally efficient, but is known to cause stability problems in certain interaction regimes, most importantly those in which the solid has very low mass. Additionally, the second-order accuracy of the central differences may be compromised by the staggered approach, rendering the method first order in time. A strong coupling integration scheme for these kinds of equations is proposed in [16] and shown to alleviate many of the stability issues. In a strongly coupled scheme the motion of the body is determined at least in part by the updated position, and thus requires iterative solving.

4.2. Spatial discretization

The Eulerian fluid domain is discretized with a staggered finite difference grid [21] with face centered velocities and cell centered pressures. Viscous terms in the Navier Stokes equations are approximated with second-order central differences. A second-order upwinding stencil is applied to the convective terms in which, for example:

$$u \frac{\partial u}{\partial x} = u^+ u_x^- + u^- u_x^+ \quad (37)$$

where at a nodal point (i, j)

$$u^\pm = 0.5(u_{i,j} \pm |u_{i,j}|), \quad (38)$$

$$u_x^- = \frac{3u_{i,j} - 4u_{i-1,j} + u_{i-2,j}}{2\Delta x}, \quad (39)$$

and

$$u_x^+ = \frac{-u_{i+2,j} + 4u_{i+1,j} - 3u_{i,j}}{2\Delta x}, \quad (40)$$

and similar expressions hold for the terms $v(\partial u/\partial y)$, $u(\partial v/\partial x)$ and $v(\partial v/\partial y)$. In some cases we will compare the effects of using first-order upwinding, in which

$$u_x^- = \frac{u_{i,j} - u_{i-1,j}}{\Delta x}, \quad (41)$$

and

$$u_x^+ = \frac{u_{i+1,j} - u_{i,j}}{\Delta x}. \quad (42)$$

The discrete values of ϕ are stored at cell centers and its spatial gradient is calculated with either ENO or WENO schemes [22], depending on the proximity of a nodal point to the domain boundary.

The discrete form of the step function $H(\phi)$ is given by

$$H^d(\phi) = \begin{cases} 0 & \phi < -\varepsilon \\ \frac{1}{2} \left(1 + \frac{\phi}{\varepsilon} + \frac{1}{\pi} \sin\left(\frac{\pi\phi}{\varepsilon}\right) \right) & |\phi| \leq \varepsilon \\ 1 & \phi > \varepsilon \end{cases} \quad (43)$$

$$\varepsilon = 1.5 * \Delta x$$

The particle boundary is defined for convenience through a second level set function, ϕ_B , and step function $H^d(\phi_B)$, where the step function is 1 in the solid domain and 0 in the fluid. The particle level set and heaviside functions are not smoothed and used for geometric tracking purposes only and are advected with the particle position rather than the level set equations. The integral of any quantity, f , over the particle domain, B embedded in a computation domain Ω may then be calculated through evaluation of

$$\int_B f \, dB = \int_{\Omega} f(x) H^d(\phi_B(x)) \, d\Omega \quad (44)$$

5. NUMERICAL RESULTS

5.1. Flow around a cylinder

A standard benchmark for flow solvers and rigid bodies is the case of a rigid cylinder in a uniform flow field for a range of Reynolds numbers. For very low Reynolds ($Re < 1$) the solution approaches Stokes flow (in a finite domain) and little separation of flow occurs downstream from the cylinder. For this case, near field analytical solutions exist for pressure distribution over the surface of the cylinder [23]. To compare against this solution, we construct a square channel [$2\text{ cm} \times 2\text{ cm}$] with a cylinder of diameter 0.2 cm and apply an inlet velocity u_{∞} at the left boundary. The right boundary has an outflow condition and symmetry is applied at the walls, that is $u_y = 0$ and $du_x/dn = 0$. The Reynolds number in this case is 0.1 . Velocity and pressure contours for a uniform grid ($\Delta x = \Delta y = 0.02\text{ cm}$) are given in Figures 2 and 3. The confined numerical solution for velocity and pressure approaches the unconfined analytical solution in the near field to the cylinder. To demonstrate this, the pressure and friction (calculated as $\mu_f(\nabla \mathbf{u} + \nabla^T \mathbf{u})$) are reconstructed on the cylinder's surface via a finite difference interpolation operator given in [24]. The solution for pressure, for example, at any Lagrangian point (ξ_k, η_k) on the boundary can be constructed from the values at surrounding nodes via

$$p_k = \Delta x \Delta y \sum_i p_i r(x_i - \xi_k) r(y_i - \eta_k) \quad (45)$$

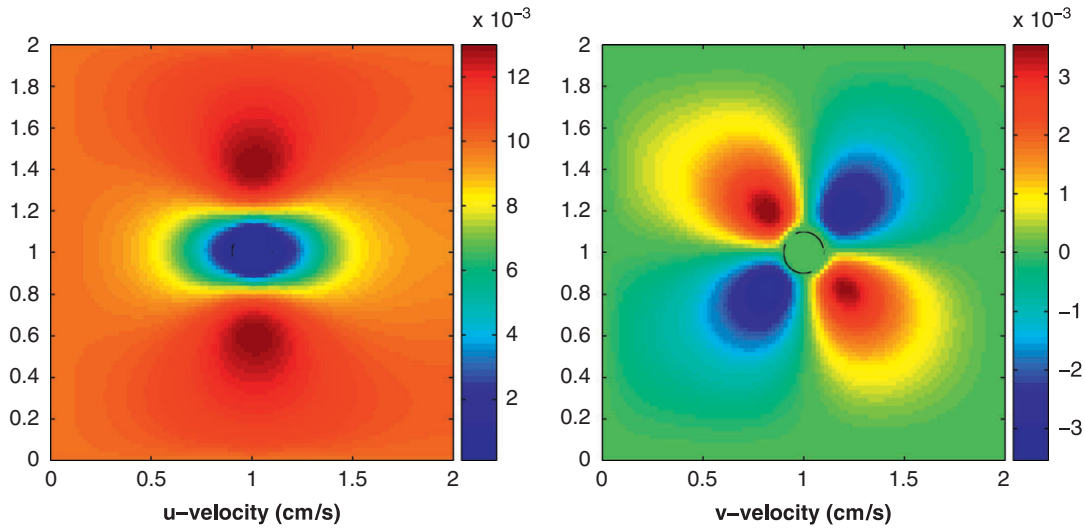


Figure 2. Velocity contours for Stokes flow around a confined cylinder.

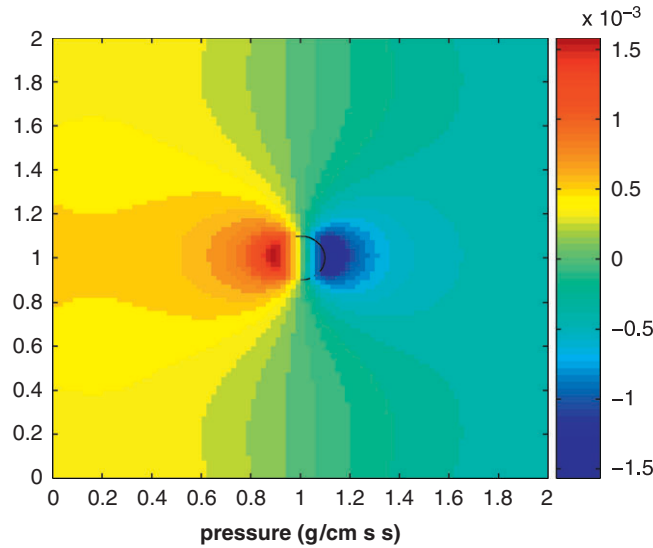


Figure 3. Pressure contours for Stokes flow around a confined cylinder.

where

$$r(d) = \begin{cases} 0 & r < -\varepsilon \\ \frac{1}{2\varepsilon} \left(1 + \cos\left(\frac{\pi r}{\varepsilon}\right) \right), & |r| \leq \varepsilon \\ 0 & r > \varepsilon \end{cases}$$

is the interpolation operator with $\varepsilon = 1.5\Delta$. The indices k and i indicate nodal points and not vector indices. Figure 4 shows the comparison of the analytical Stokes flow surface pressure and friction distribution versus numerical results.

To study the behavior of the system (wake formation and vortex shedding) at higher Reynolds numbers, the numerical domain is extended to a long channel, $[2\text{ cm} \times 10\text{ cm}]$. The boundary conditions remain the same. As the Reynolds number increases, separation of the flow occurs and a

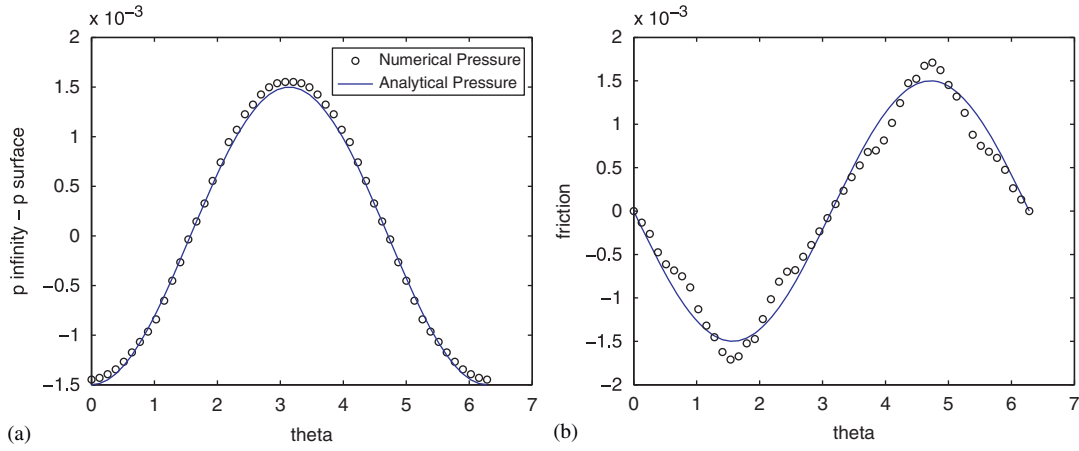


Figure 4. Surface pressures and friction for a confined cylinder in Stokes flow.

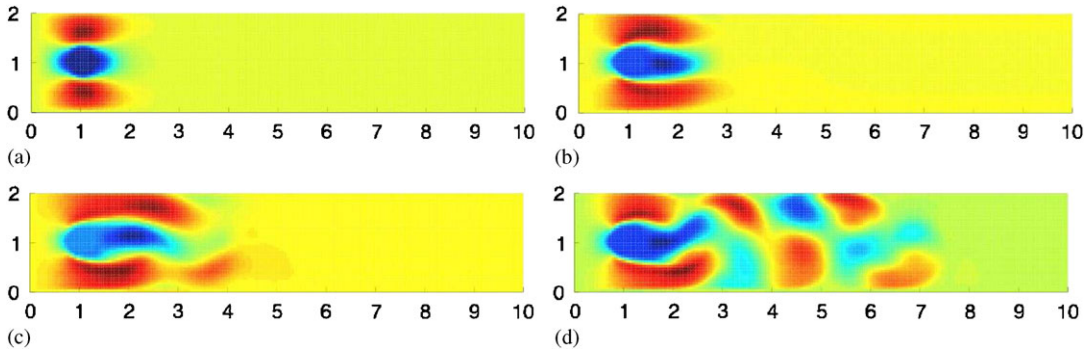


Figure 5. Wake formation and vortex flow over a cylinder for (a) $Re=5$; (b) $Re=50$; (c) $Re=100$; and (d) $Re=200$. Time = 3 s. u -velocity is shown.

Table I. Drag coefficient for the current study versus the literature benchmarks.

Re	Current	[25]	[26]	[27]
5	4.32	4.42		
50	1.60	1.74	1.38	1.81
100	1.60	1.46	1.26	1.76
200	1.58	1.29	1.18	1.76

stable laminar vortex appears in the wake of the cylinder (Figure 5). Von Karman vortex shedding is known to occur at Reynolds numbers for this case starting around $Re=45$.

Lift and drag coefficients in this case are an important measure of the accuracy of an algorithm. The lift and drag coefficients, C_L and C_D respectively are calculated as

$$C_{(L \text{ or } D)} = \frac{F_{(L \text{ or } D)}}{0.5\rho_f U_\infty^2 d} \quad (46)$$

where d is the diameter of the cylinder. F_L and F_D are the total lift and drag forces, which can be calculated via the total traction acting on the cylinder at a given time:

$$F_L = \int_0^{2\pi} |\sigma_f \cdot \mathbf{n}| \sin(\theta) d\theta \quad \text{and} \quad F_D = \int_0^{2\pi} |\sigma_f \cdot \mathbf{n}| \cos(\theta) d\theta \quad (47)$$

where θ is measured from the stagnation point. For Reynolds numbers higher than $Re=40$, C_L and C_D are time dependent. Time-averaged values for drag coefficient are given in Table I and

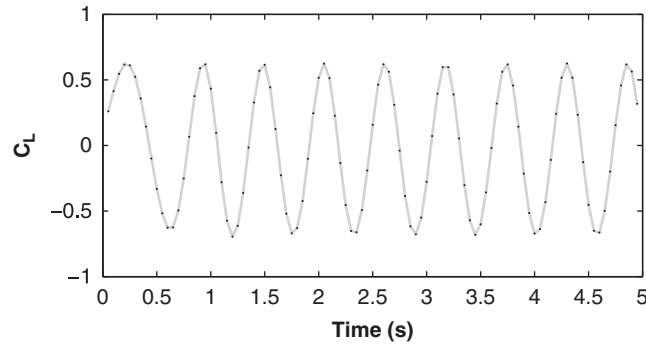


Figure 6. Lift coefficient versus time for flow around a fixed circular cylinder for $Re=200$.

compared with the standard literature numerical and experimental results. A plot of lift coefficient versus time for $Re=200$ is given in Figure 6.

5.2. Sedimentation and rising of a cylindrical disk

A second numerical problem that includes rigid body dynamics and has been extensively studied is that of the sedimentation of a circular disk. Construction of the problem is done in such a way that it matches numerical studies from the Distributed Lagrange Multiplier approach [9] and IFEM [6] approaches. A cylinder of 0.25 cm radius starts at rest in the center of a 2D channel with width 2 cm and length 6 cm. The fluid properties approximate water, with a density of $\rho_f = 1.0(\text{g/cm}^3)$ and viscosity $\mu_f = 0.01(\text{g/cm} \cdot \text{s})$. The solid has a density $\rho_s = 1.2(\text{g/cm}^3)$ and will accelerate downwards in the fluid until viscous drag forces balance gravity and a terminal velocity is reached. Velocity and pressure contours for the fluid domain with a uniform grid ($\Delta x = \Delta y = 0.04$ cm) are given in Figure 7. Figure 8 shows reasonable agreement with the previous studies for the time history of position and velocity of the rigid particle.

A more challenging problem in terms of stability, especially for loosely coupled time integration schemes, is that in which a solid that is less dense than a surrounding fluid rises due to buoyancy effects. Thus, the problem was repeated but with the cylinder starting at rest at $y=2.0$ cm and a density of $\rho_s = 0.8(\text{g/cm}^3)$. Figure 9 shows three different velocity profiles of the cylinder as it rises in the fluid, corresponding to successively finer grids. Figure 10 shows the final upwards 'terminal' velocity to be consistently converging to a stable solution (given by an appropriately refined reference grid).

5.3. Rigid body in a two-phase fluid: buoyancy

One example of the motion of a rigid body in a two-phase fluid is the decaying oscillation of a buoyant body on a free surface. There have been analytical and numerical studies to provide benchmarks [28, 29] and in this case we study a circular cylinder in a tank of water and air, with density half that of water such that the buoyant equilibrium point is approximately half submerged (the density of air being 1000 times smaller does comparatively little to change the final equilibrium position). To match the simulations of [29], which treated non-linear free-surface/rigid body interaction with an implicit boundary element technique, a cylinder with radius 2 m is positioned in a tank of 50 m in length with rigid walls and a no-slip condition at the ends (a condition that allows reflected waves). The depth of the tank is 4 m. The initial position of the cylinder's center of mass is 0.5 m above the free surface. The liquid phase has properties of water with $\rho = 1000(\text{kg/m}^3)$, $\mu = 0.001(\text{kg/m} \cdot \text{s})$, and the gas phase has properties of air with $\rho = 1(\text{kg/m}^3)$, $\mu = 0.00002(\text{kg/m} \cdot \text{s})$. Results are shown in comparison to those from [28, 29] in Figure 11 for a grid size of $\Delta x = \Delta y = 0.3$ m. In both the current and previous numerical studies the heave motion of the cylinder decays over a 10-s simulation period and the center of mass

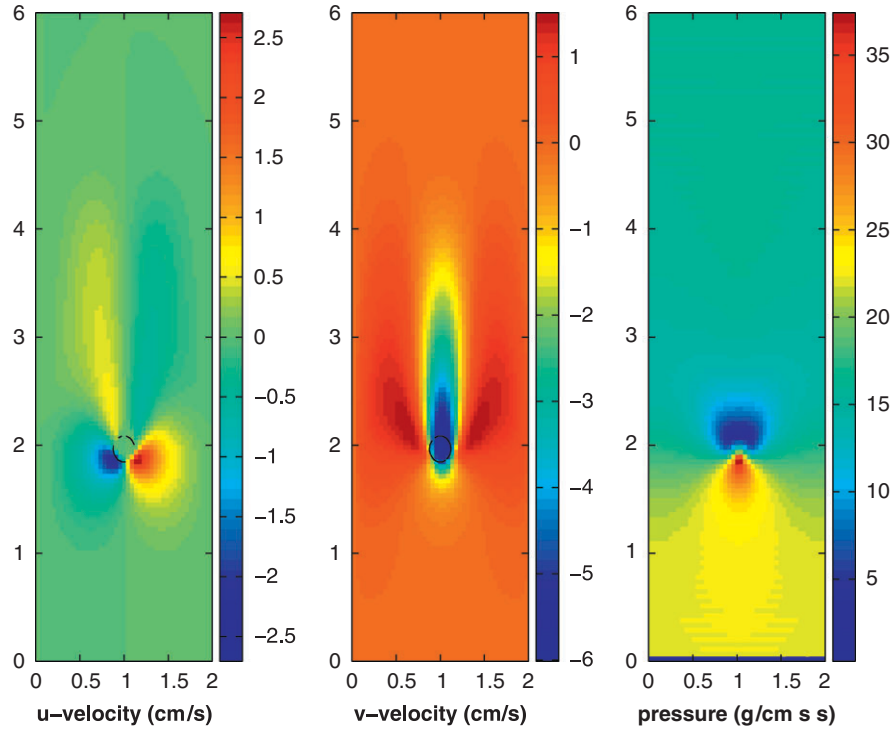


Figure 7. Velocity and pressure (minus hydrostatic pressure) contours for sedimentation of a cylindrical disk at $t=0.4s$.

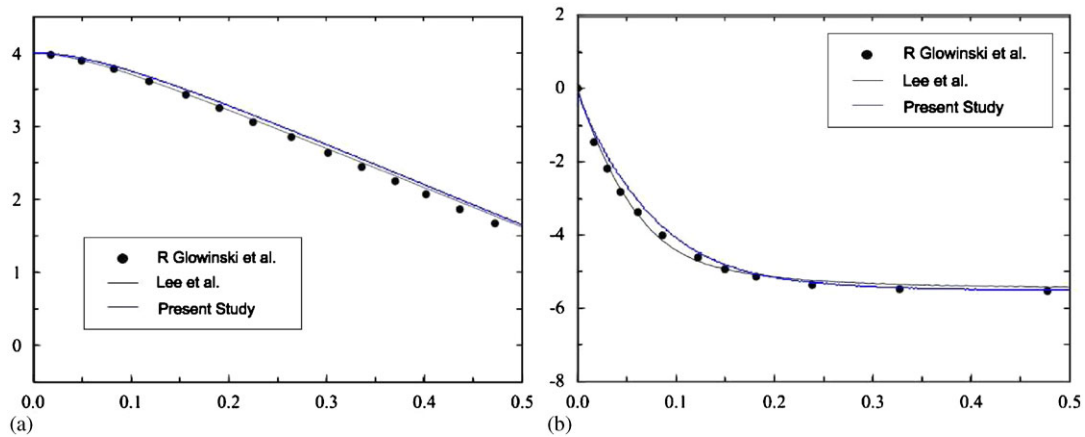


Figure 8. Position and velocity of disk as a function of time versus benchmark solutions for sedimentation of a cylindrical disk.

settles to the predicted position (indicated by the dotted line) based on buoyancy. The Reynolds number in this case can be defined [30] by

$$Re = \frac{\rho_{\text{water}} \sigma D^2}{\mu_{\text{water}}} \quad (48)$$

where σ is the frequency of vertical heave and D is the diameter. For this example $Re \approx 8e6$.

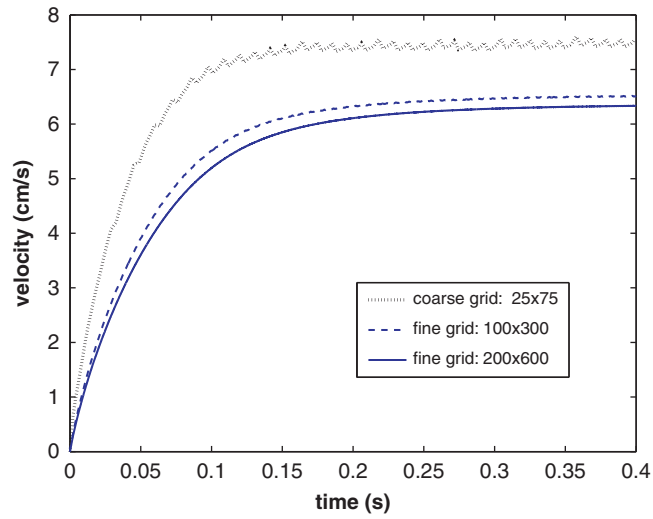


Figure 9. Velocity profiles for a buoyant cylinder in successively finer grids.

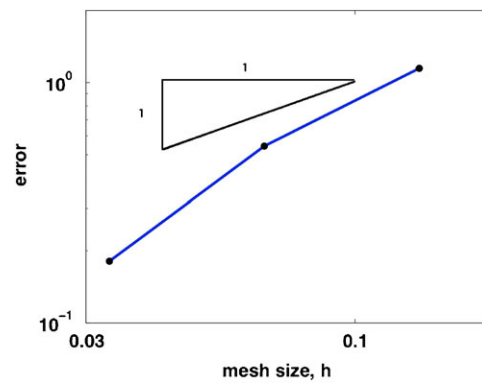


Figure 10. Error in terminal velocity for a buoyant cylinder. The error decreases at an order slightly greater than 1. A fine grid with a spatially converged solution is used as the reference solution.

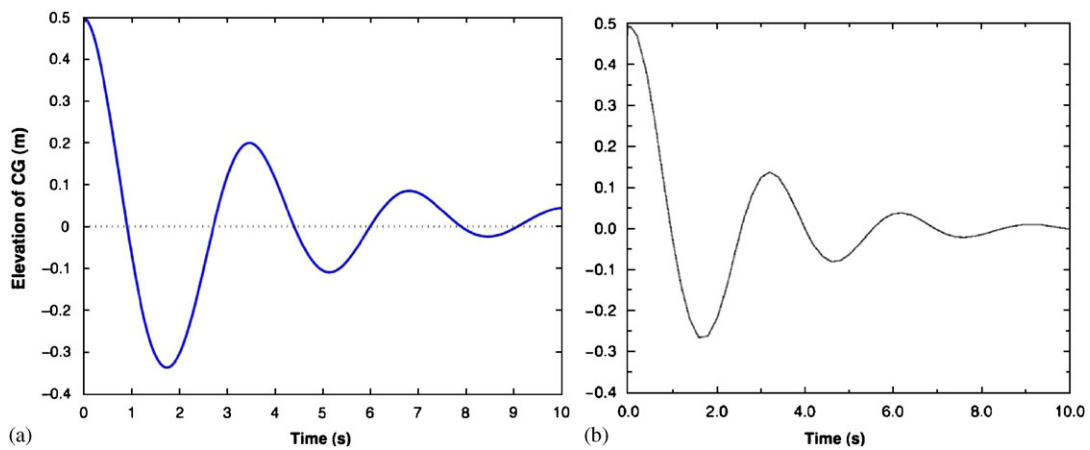


Figure 11. Decay of heave for a buoyant cylinder for (a) the current study and (b) [29].

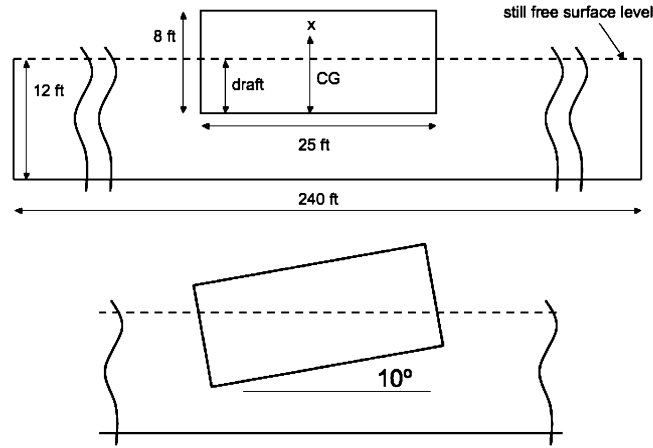


Figure 12. Physical dimensions of barge shape for roll calculations.

For the numerical results of [29] the damping ratio is approximately 0.19, and in our numerical results it is slightly less (0.15). The damping ratio is calculated as

$$Z = \frac{d}{\sqrt{(2\pi)^2 + d^2}} \quad (49)$$

where d is the logarithmic decrement of two successive periods of oscillation, T_1 and T_2 :

$$d = \ln\left(\frac{T_1}{T_2}\right). \quad (50)$$

A parametric study of the problem shows that the two greatest factors that affect the damping ratio are the value of gravity and water depth, with a deeper basin decreasing the damping ratio.

5.4. Roll of a buoyant body

The in-plane rotation (or roll) of a buoyant body can represent a large part of the total motion, and has the potential to have a profound impact on the energetic uptake of wave energy harvesters. Decades of research from the ship capsize community [31] has shown that heave and roll are strongly coupled motions under wave excitations for non-axisymmetric bodies.

Experimental and two-dimensional numerical results from a study of free decay of roll motion for a barge [32, 33] in a wave basin provide a suitable benchmark for the roll of an oblong object, and are repeated with the current method.

The shape of the barge, with dimensions, is shown in Figure 12. The water depth is set to 12 ft and two different values for draft, or the distance from the still water line to the barge depth, are used (4 and 6 feet). In addition, three different values of center of gravity (CG) and radius of gyration (RG) are used, giving a total of six test cases, A1–B3. Radius of gyration is related to the rotational inertia of the barge through the relationship $I = m(RG)^2$. Natural roll periods are determined for the six cases by giving the body an initial angle of 10° from horizontal. The liquid phase has properties of water with $\rho = 62(\text{lb}/\text{ft}^3)$, $\mu = 1.8 \times 10^{-5}(\text{lb s}/\text{ft}^2)$, and the gas phase has properties of air with $\rho = 0.062(\text{lb}/\text{ft}^3)$, $\mu = 3.6 \times 10^{-7}(\text{lb s}/\text{ft}^2)$. Results are reported for a grid size of $\Delta x = \Delta y = 0.65$ ft.

Results for the natural roll frequencies, compared with the numerical calculations of [33] and original experimental data from [32], are given in Table II. Additionally, the time history of the roll angle of the barge is shown for one example case (A1) in comparison to the previous numerical study (Figure 13) with both second- and first-order upwinding. It can be seen that the current study is once again slightly less dispersive than previous numerical studies. The slight blip in the

Table II. Experimental and numerical comparisons of decaying roll frequencies for six cases.

Case	A1	A2	A3	B1	B2	B3
Draft (ft)	4.0	4.0	4.0	6.0	6.0	6.0
CG (ft)	9.13	10.23	11.18	9.24	10.33	11.30
RG (ft)	10.31	10.41	10.09	10.11	10.23	10.11
Exp roll period (s)	5.4	5.9	6.5	7.3	8.9	12.3
Num roll period (s)	5.73	6.18	6.76	8.01	10.36	15.69
Current study (s)	5.36	5.80	6.26	7.12	8.4	11.86

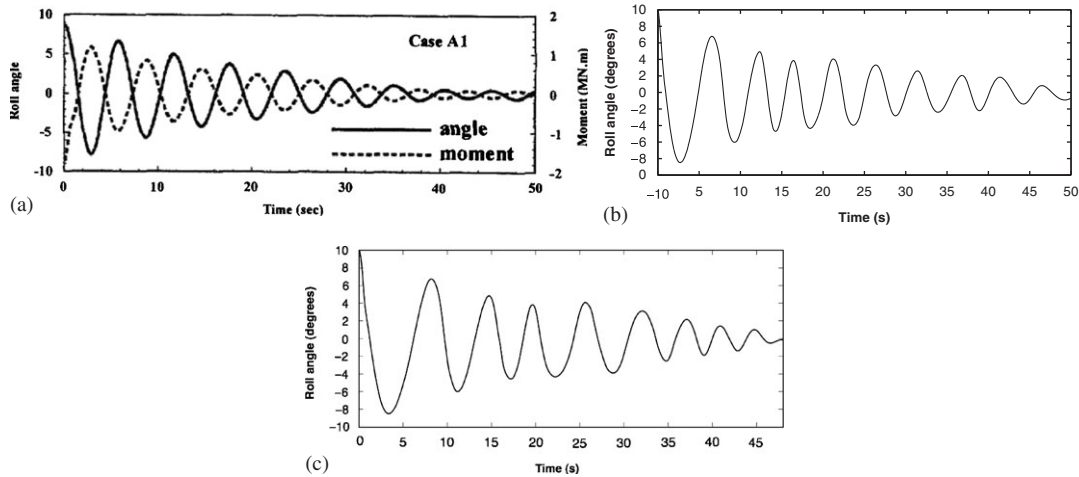


Figure 13. Example time histories of free decay of ship roll motion for previous (a) and current studies with second-order (b) versus first-order upwinding (c).

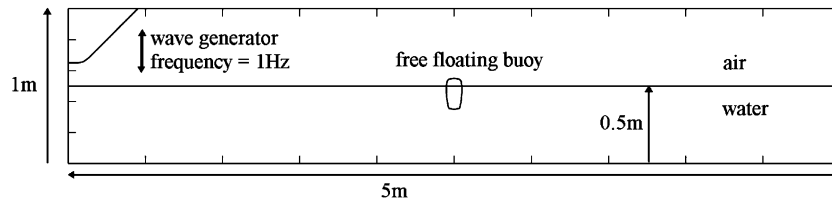


Figure 14. Setup for wave tank simulation problem.

consistent decay of the roll angle at $t=20$ s comes from the influence of reflected waves in the current study.

The Reynolds number in these cases range from $Re=2e5$ to $Re=6e5$.

5.5. Wave tank and buoy simulations

The goal of the presented algorithm will be to compare numerical results with a scale wave tank with buoy prototypes to replicate energy harvesting systems. The simulated wave tank is 5 m long with a water depth of 0.5 m. A wedge-shaped wave generator with variable frequency oscillates at one end. The motion of a buoy with a height of 20 cm, width of 10 cm, weight of 15 g, and center of gravity 5 cm below the geometric center, is studied under steady-state conditions generated in the tank with the wave generator moving at 1 Hz. The numerical domain is shown in Figure 14. Single time snapshots of the simulation are shown in Figure 15, with closeups of the buoy shown at the same times in Figure 16 and a time history of the heave of the cylinder is given in Figure 17.

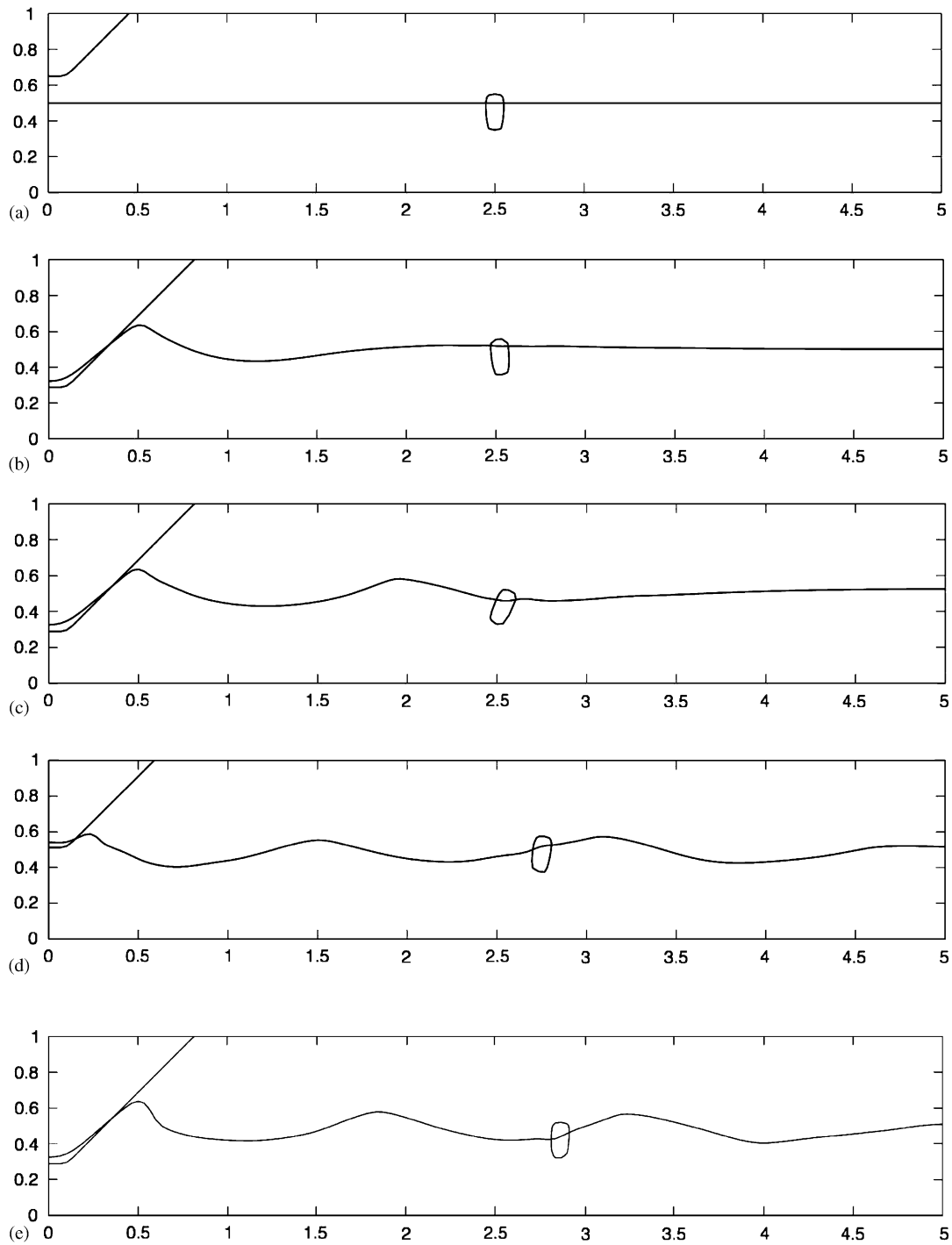


Figure 15. Snapshots of wave tank simulations at $t = 0.0, 1.4, 2.4, 5.2$ and 8.4 s.

6. CONCLUSION

A numerical method has been presented for the simulation of the two-dimensional motion of rigid bodies and their interactions with two-phase incompressible flow and large amplitude-free surface motion. The method uses a finite difference approach to the two-phase fluid problem that takes advantage of the current level of sophistication of the level set method. However, the standard

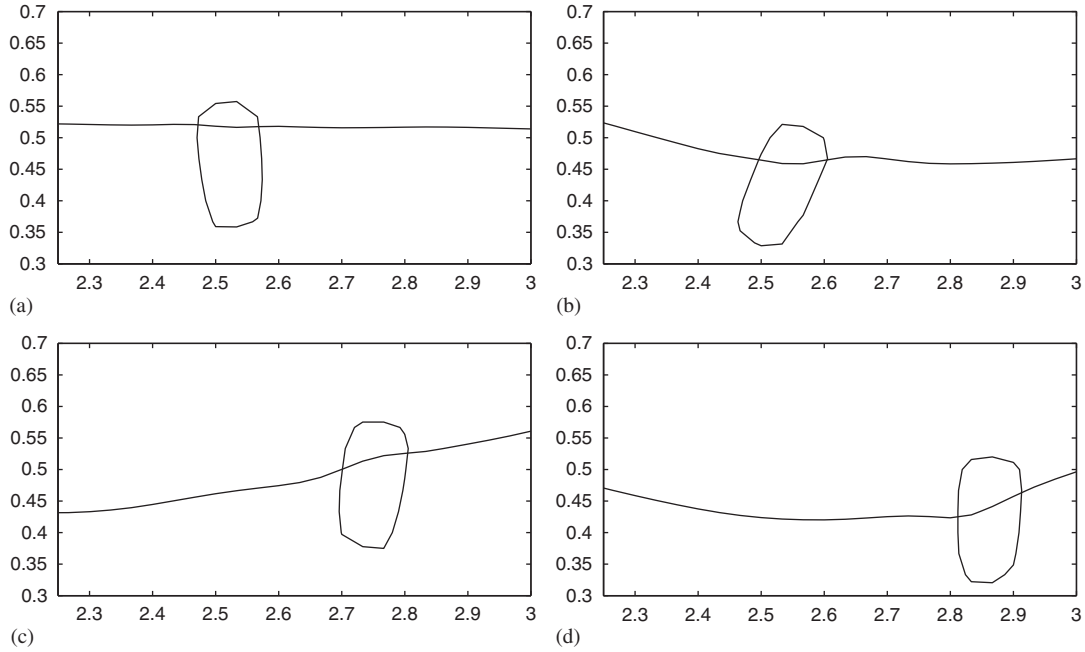


Figure 16. Zoomed in snapshots of wave tank simulations at $t = 1.4, 2.4, 5.2$ and 8.4 s.

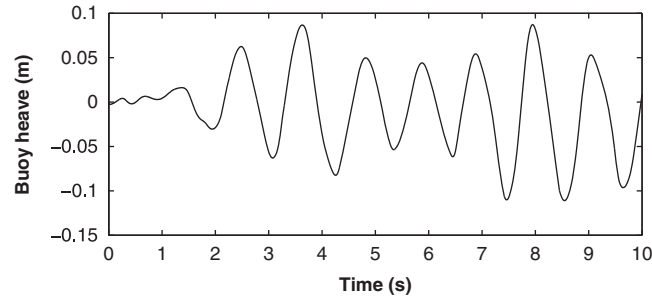


Figure 17. Heave motion of center of mass of a free floating buoy in wave tank.

paradigm for tracking solid motion in a fluid, that is to say, solving for solid motion on a fluid grid, has been abandoned in favor of a Lagrangian approach to rigid body motion, in order to facilitate the anticipated addition of internal dynamics to the solid equations of motion, as well as make the method more easily extensible to problems where material deformation may be important to rigorously resolve. The current method shows a good agreement with standard benchmarks. For the full resolution of off-shore flows, it is anticipated that the method will be further benchmarked in 3D. Additional work will involve the integration of internal dynamics into the algorithm, and comparison to wave tank data. The two-phase solver can additionally be improved through the use of the relatively new Coupled Level Set Volume of Fluid (CLSVOF) method [34], which has been shown to greatly improve the volume conserving properties of the level set method.

ACKNOWLEDGEMENTS

The authors acknowledge the support of the Air Force Office of Scientific Research Contract FA9550-06-1-0108 (TAL, JED and JS), and the Department of Defense National Defense Science and Engineering Fellowship Program (JS). PJM's participation was supported by the NSF (DMS-0645369).

REFERENCES

1. Peskin CS. Numerical analysis of blood flow in the heart. *Journal of Computational Physics* 1977; **25**: 220–252.
2. Legay A, Chessa J, Belytschko T. An Eulerian–Lagrangian method for fluid–structure interaction based on level sets. *Computer Methods in Applied Mechanics and Engineering* 2006; **195**:2070–2087.
3. Zhang L, Gerstenberger A, Wang X, Liu WK. Immersed finite element method. *Computer Methods in Applied Mechanics and Engineering* 2004; **85**:2051–2067.
4. Zhao H, Freund JB, Moser RD. A fixed-mesh method for incompressible flow–structure systems with finite solid deformations. *Journal of Computational Physics* 2008; **227**:3114–3140.
5. Sussman M, Puckett EG. A level set approach for computing solutions to incompressible two-phase flow. *Journal of Computational Physics* 1994; **114**:146–159.
6. Lee TR, Chang YS, Choi JB, Kim DW, Liu WK, Kim YJ. Immersed finite element method for rigid body motions in the incompressible Navier–Stokes flow. *Computer Methods in Applied Mechanics and Engineering* 2008; **197**:2305–2316.
7. Zhang L, Gay M. Imposing rigidity constraints on immersed objects in unsteady flow. *Computational Mechanics* 2008; **42**:357–370.
8. Glowinski R, Pan TW, Hesla TI, Joseph DD. A distributed Lagrange multiplier/fictitious domain method for particulate flows. *International Journal of Multiphase Flow* 1999; **25**:755–794.
9. Glowinski R, Pan TW, Hesla TI, Joseph DD, P  riaux J. A fictitious domain approach to the direct numerical simulation of incompressible viscous flow past moving rigid bodies: application to particulate flow. *Journal of Computational Physics* 2001; **169**:363–426.
10. Sharma N, Patankar N. A fast computation technique for the direct numerical simulation of rigid particulate flows. *Journal of Computational Physics* 2005; **205**:439–457.
11. Carlson M, Mucha P, Turk G. Rigid fluid: animating the interplay between rigid bodies and fluid. *ACM SIGGRAPH Conference Proceedings*, Los Angeles, California, 2004.
12. Takahashi T, Ueki H, Kunimatsu A, Fujii H. The simulation of fluid–rigid body interaction. *ACM SIGGRAPH*, San Antonio, Texas, 2002.
13. Batty C, Bertails F, Bridson R. A fast variational framework for accurate solid–fluid coupling. *ACM SIGGRAPH*, San Diego, California, 2007.
14. Chentanez N, Goktekin TG, Feldman BE, O’Brien JF. Simultaneous coupling of fluids and deformable bodies. *Proceedings of the 2006 ACM Siggraph/Eurographics Symposium on Computer Animation*, 2006.
15. Kim D, Choi H. Immersed boundary method for flow around an arbitrarily moving body. *Journal of Computational Physics* 2006; **212**:662–680.
16. Borazjani I, Ge L, Sotiropoulos F. Curvilinear immersed boundary method for simulating fluid structure interaction with complex 3D rigid bodies. *Journal of Computational Physics* 2009; **227**:7587–7620.
17. Sussman M. A second order coupled level set and volume of fluid method for computing growth and collapse of vapor bubbles. *Journal of Computational Physics* 2003; **187**:110–136.
18. Morgan NR. A new liquid–vapor phase transition technique for the level set method. *Ph.D. Dissertation*, Georgia Institute of Technology, 2007.
19. Chorin AJ. Numerical solution of the Navier–Stokes equations. *Mathematics of Computation* 1968; **104**: 745–762.
20. Simo JC, Wong KK. Unconditionally stable algorithms for rigid body dynamics that exactly preserve energy and momentum. *International Journal for Numerical Methods in Engineering* 1991; **31**:19–52.
21. Harlow FH, Welsh JE. Numerical calculation of time-dependent viscous incompressible flow of fluid with free surface. *Physics of Fluids* 1965; **8**:2182–2189.
22. Jiang GS, Peng G. Weighted ENO schemes for Hamilton Jacobi equations. *SIAM Journal on Scientific Computing* 2000; **21**:2126–2143.
23. Wagner GJ, Mo  s N, Liu WK, Belytschko T. The extended finite element method for rigid particles in Stokes flow. *International Journal for Numerical Methods in Engineering* 2001; **51**:293–313.
24. Taira K, Colonius T. The immersed boundary method: a projection approach. *Journal of Computational Physics* 2007; **225**:2118–2137.
25. White F. *Viscous Fluid Flow*. McGraw-Hill: New York, 1991.
26. Saiki EM, Biringen S. Numerical simulation of a cylinder in uniform flow: application of a virtual boundary method. *Journal of Computational Physics* 1996; **123**:450–465.
27. Gresho P. Incompressible fluid dynamics: some fundamental formulation issues. *Annual Review of Fluid Mechanics* 1991; **23**:413–453.
28. Zandbergen PJ, Broeze J, van Daalen EFG. A panel method for the simulation of nonlinear gravity waves and ship motions. In *Advances in Boundary Element Techniques*, Kane JH, Maier G, Tosaka N, Atluri SN (eds). Springer: Berlin, 1993; 486–509.
29. Donescu P, Virgin L. An implicit boundary element solution with consistent linearization for free-surface flows and non-linear fluid–structure interaction of floating bodies. *International Journal for Numerical Methods in Engineering* 2001; **51**:379–412.
30. Yeung RW, Ananthakrishnan P. Oscillation of a floating body in a viscous fluid. *Journal of Engineering Mathematics* 1992; **26**:211–230.

31. Liaw CY, Bishop SR. Nonlinear heave-roll coupling and ship rolling. *Nonlinear Dynamics* 1995; **8**:197–211.
32. Chen HC, Liu T, Huang E. Stability investigation of a pontoon barge in wave basin. *Proceedings of the Eleventh International Offshore and Polar Engineering Conference*, Stavanger, Norway, 2001.
33. Chen HC, Liu T, Huang E. Time-domain simulation of large amplitude ship roll motions by a Chimera RANS method. *Proceedings of the Eleventh International Offshore and Polar Engineering Conference*, 2001.
34. Sussman M, Puckett EG. A coupled level set and volume-of-fluid method for computing 3D and axisymmetric incompressible two-phase flows. *Journal of Computational Physics* 2000; **162**:301–337.